






RESEARCH ARTICLE | AUGUST 17 2023

A novel experimental approach to measure nebulized droplet deposition pattern and deposition fraction in an idealized mouth-to-throat model **FREE**

Yi Jin (金怡); Xiaole Chen (陈晓乐) ; Yu Feng (冯宇) ; Zhenning Jia (贾振宁) ; Jinan Zhang (张金安) ; Xiaojian Xie (解晓健) ; Ya Zhang (张亚)



Physics of Fluids 35, 083322 (2023)

<https://doi.org/10.1063/5.0163935>



View
Online



Export
Citation

CrossMark

Articles You May Be Interested In

Aerosol particle transport and deposition in a CT-scan based mouth-throat model

AIP Conference Proceedings (July 2019)

A novel experimental approach to measure nebulized droplet deposition pattern and deposition fraction in an idealized mouth-to-throat model

Cite as: Phys. Fluids **35**, 083322 (2023); doi: 10.1063/5.0163935

Submitted: 20 June 2023 · Accepted: 1 August 2023 ·

Published Online: 17 August 2023



View Online



Export Citation



CrossMark

Yi Jin (金怡),¹ Xiaole Chen (陈晓乐),^{1,a)}  Yu Feng (冯宇),²  Zhenning Jia (贾振宁),³  Jinan Zhang (张金安),¹ 
Xiaojian Xie (解晓健),¹  and Ya Zhang (张亚)⁴

AFFILIATIONS

¹School of Energy and Mechanical Engineering, Nanjing Normal University, Nanjing, Jiangsu 210042, China

²School of Chemical Engineering, Oklahoma State University, Stillwater, Oklahoma 74078, USA

³Vapo Healthcare Co., Ltd, Suzhou, Jiangsu 510765, China

⁴Department of Otolaryngology Head and Neck Surgery, The Second Affiliated Hospital of Xi'an Jiaotong University, Xi'an, Shaanxi 710004, China

^{a)} Author to whom correspondence should be addressed: xlcn@njnu.edu.cn

ABSTRACT

Accurate measurement of droplet/particle deposition fraction and spatial distribution is vital for understanding various inhalation processes, including nebulized therapy, inhalation of atmospheric pollutants, and exposure risk assessment to aerosols such as airborne SARS-COV-2-laden droplets. This paper presents a novel method to measure the deposition fraction and spatial distribution of the deposited particulate phase (i.e., deposition pattern) of droplets through a single experiment. The experiment employs an idealized mouth-to-throat model as a test platform for two vibrating mesh nebulizers to deposit droplets. By utilizing a nebulized solution of normal saline containing the fluorescein, the qualitative observation of droplet deposition pattern on the internal surfaces is achieved under ultraviolet excitation. Furthermore, through rinsing the experimental components and quantitatively determining the deposition fraction based on rinsate absorbance, experimental results indicate that the deposition fraction of nebulized droplets decreases initially and then increases with increasing inspiratory flow rate from 15 to 60 l/min. Additionally, the deposition hotspots gradually shift from the bottom of the oral cavity to the throat as the inhalation flow rate increases. In addition to providing validation data for the transport and deposition of high-concentration droplets, this experimental method has the potential for extension to research on aerosol transmission and exposure risk assessment. It offers valuable insight into the behavior of nebulized droplets, aiding in developing effective strategies for aerosolized therapies and mitigating transmission risks in various applications.

Published under an exclusive license by AIP Publishing. <https://doi.org/10.1063/5.0163935>

I. INTRODUCTION

Inhalation therapy serves as the primary method for managing chronic obstructive pulmonary disease (COPD) and asthma.^{1,2} It involves the use of various inhalation devices such as metered-dose inhalers (MDIs), dry powder inhalers (DPIs), and nebulizers.^{3,4} Among these devices, nebulizers stand out due to their lower demands for hand-mouth coordination and inhalation flow rate, making them particularly user-friendly for elderly and pediatric patients.⁵⁻⁷ Furthermore, vibrating mesh nebulizers (VMNs) are more portable and operate silently, making them increasingly popular over

traditional ultrasonic and jet nebulizers. As a result, the market share of VMNs has been steadily increasing over the past few years.⁸⁻¹¹ Due to VMNs' ability to preserve vaccine bioactivity, they have garnered significant attention during the COVID-19 pandemic as potential delivery devices for inhalable vaccines.¹²

The generation, transport, and deposition of droplets in the respiratory tract using VMNs involve complex fluid dynamics as well as heat and mass transfer phenomena.¹³ Droplet generation in VMNs relies on the principle of a micro-pump, where liquid is retained on one side of a vibrating plate containing conical orifices due to surface

tension. Vibrations driven by high-frequency voltage force the liquid through the orifices on the liquid-facing side, expelling droplets into the air.¹⁴ Figure 1 depicts the process for droplet generation. Therefore, such a process is related to fundamental research on fluid motion subject to fluid–structure coupling, fluid flow through micro-scale holes with varying diameters, and droplet bouncing dynamics on vibrating surfaces.^{15–17}

The transport and deposition of droplets in the respiratory tract are influenced by intricate airflow patterns resulting from the complex geometric structure and abrupt changes in cross-sectional areas of the airways.^{18,19} As air flows from the mouth to the throat, the airway's cross section experiences sudden reductions, followed by increases near the pharynx and throat, leading to laminar-to-turbulence transition and jetting.²⁰ The complex flow regime induces intricate and strong phase change dynamics between inhaled droplets and water vapor. As inhaled air travels through the respiratory tract, it undergoes humidification and warming processes. Multicomponent droplets, which may contain water, NaCl, and soluble or insoluble forms of medications, experience evaporation within the varying temperature and humidity fields along the respiratory tract.²¹ Inhaled droplets can absorb moisture and increase in the size and mass near the mucus layer even after evaporating into dry particles, ultimately leading to deposition onto the mucus.

Both *in vivo* and *in vitro* studies have consistently demonstrated the advantages of VMNs over traditional nebulizers. The Single Photon Emission Computed Tomography (SPECT)–CT analysis revealed that using a VMN combined with a valved holding chamber in six healthy male subjects can lead to a lung deposition efficiency six times higher than a traditional jet nebulizer.²² Additionally, Waldrep and Dhand²³ discovered that VMNs enhanced drug delivery efficiency compared to traditional nebulizers, particularly for mild to moderate asthmatics. In an idealized mouth-to-throat (MT) model study, the deposition efficiency of inhaled aerosols using a commercial VMN was quantified, revealing that under the condition of 15 l/min, the lung deposition efficiency of the VMN reached approximately 60%.²⁴

Due to the significant subject variability among volunteers, including factors such as gender, age, weight, and breathing pattern, *in vivo* human studies often encounter challenges in obtaining consistent results. Therefore, *in vitro* experiments assume significant importance as they provide a controlled and reproducible environment, thus mitigating the challenges associated with subject variability. For instance, Park *et al.*²⁵ evaluated the delivery efficiency of six different nebulizers, including two jet nebulizers, two static mesh nebulizers, and two VMNs under different breathing patterns. However, it is

worth noting that the measurement of the delivery dose in this study was conducted directly using filter membranes, without employing a respiratory tract physical model for lung deposition quantification. Gürzing *et al.*²⁶ conducted *in vitro* experiments in an in-plane transparent airway model to investigate the transport characteristics of liquid bronchoscopic spray in the bronchi. They employed laser-induced fluorescence to capture the dynamics of liquid transport, including the formation of liquid films and plug flow. Most recently, Xia *et al.*²⁷ introduced a novel approach that involves the washing and measuring of solution ion concentrations after droplet deposition experiments. This method aims to determine the deposition fraction (DF) of droplets generated by VMNs in an idealized MT model. However, the abovementioned *in vitro* studies are not able to visualize local deposition patterns of the inhaled aerosols simultaneously using the same experiment.

The deposition pattern describes the spatial distribution of droplets/particles and provides a visual representation of the dense deposition regions. There are limited experimental measurement methods available for characterizing deposition patterns. For instance, Finlay *et al.*²⁸ employed a semi-quantitative approach to determine the deposition pattern of di-ethylhexyl sebacate oil (DEHS) aerosol labeled with ^{99m}Tc. They visualized the deposition pattern using a single photon emission gamma camera, enabling the calculation of the deposition fraction for each specific region. Su and Cheng²⁹ performed carbon fiber deposition experiments in two human respiratory tract replicas. After the experiments, they dissected the respiratory tract replicas into regions and captured images to highlight the hotspots where the carbon fibers deposited. The high contrast between the respiratory tract model and the carbon fibers facilitated this visualization. Sakai *et al.*³⁰ utilized the laser-induced fluorescence method to measure the deposition locations of lycopodium powder doped with fluorescent dye in a transparent nasal cavity model. Laser-induced fluorescence is also used to capture the liquid breakup and spray evolution.^{31–33} Xi *et al.*³⁴ utilized Sar-Gel to coat the inner surface of the respiratory tract to characterize the deposition patterns of droplets generated by different nebulizers. The observed deposition patterns were found to be consistent with the deposition patterns predicted by numerical simulations.

Similarly, when assessing exposure risk induced by aerosol transmission, tracer gases, such as SF₆ and N₂O,^{35,36} as well as particles of different diameters,³⁷ are widely used to measure the deposition or inhalation of aerosolized particles on infected individuals. Nevertheless, a notable gap remains in terms of reliable experimental methods for directly observing the deposition pattern of exhaled droplets or particles.

The importance of accurately determining deposition fractions and spatial distribution of droplets/particles in specific environments, particularly in the context of the COVID-19 pandemic, cannot be overstated.^{38,39} This information plays a crucial role in comprehending the transmission dynamics of hazardous aerosols and designing mitigation strategies.^{40,41} However, there is currently a scarcity of methods that can simultaneously provide deposition fractions and patterns within relatively small geometric spaces like the respiratory tract. Addressing this gap is essential for advancing our knowledge and enhancing the efficacy of preventive measures.⁴²

To bridge the aforementioned gap, this study presents a novel experimental method that enables simultaneous measurement of

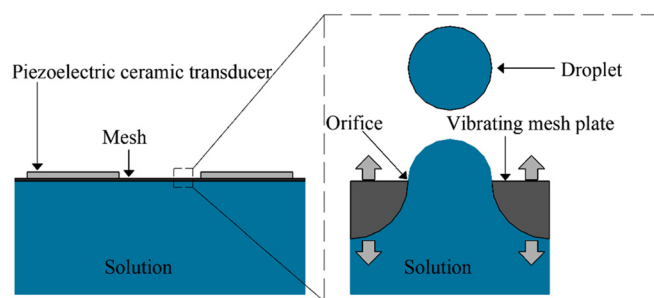


FIG. 1. Schematic illustration of droplet generation process in VMNs.

deposition fractions and deposition patterns of droplets within an idealized MT respiratory tract model. To the best of our knowledge, this method represents a pioneering experimental approach that enables simultaneous acquisition of regional and local deposition information. In this experiment, two VMNs are utilized to generate a large number of droplets by nebulizing a fluorescein-containing normal saline solution. The idealized MT model serves as the test bed for conducting the deposition experiments. Following the deposition experiment, the internal surface of the MT model is irradiated with ultraviolet (UV) light, causing the droplets to fluoresce to facilitate the visualization of the deposition patterns. Additionally, the experimental components undergo thorough cleaning, and the absorbance of the rinsate is quantified to determine the deposition fractions. The study reveals that the deposition patterns and deposition fractions of nebulized droplets exhibit significant variations with changes in inspiratory flow rates. The results provide benchmark experimental data for validating numerical simulations of multi-component droplet transport, evaporation/condensation, and deposition. Moreover, this innovative method holds promise for further applications in human exposure risk assessment of aerosols.

II. METHOD

A. Experimental setup

The experiments were performed in an ISO (International Organization for Standardization) 4 cleanroom with temperature and relative humidity (RH) set at $26.5^{\circ}\text{C} \pm 1^{\circ}\text{C}$ and $50\% \pm 2\%$, respectively. The particle concentration in the ISO 4 cleanroom was verified by a TSI Optical Particle Size Spectrometer 3330 (TSI, Inc., MN). As depicted in Fig. 2, the experiment setup consisted of a VMN, an idealized MT model, a bubble absorption tube, a prefilter, a membrane filter, a glass rotor flowmeter (10–100 l/min, $\pm 4\%$, LZM-6T, Senlod Co., Ltd., Nanjing, China), and a vacuum pump. A silicone mouthpiece was used to connect the VMN and the MT model.

Two customized VMNs were used in this study. The VMN bodies were 3D-printed, and the mesh plates had different numbers of orifices, i.e., 700 and 1200. The mesh plate with 700 orifices was identical to the one used in a commercial product (VP-M1, Vapo Healthcare Co., Ltd., Jiangsu, China). The mesh plate with 1200 orifices was customized by Vapo Healthcare Co., Ltd. Each mesh plate was vertically installed on the body of the VMN (see Fig. 3) and connected to a circuit board, also from the VP-M1. The VMNs equipped with 700 orifices and 1200 orifices were designated VMN1 and VMN2, respectively.

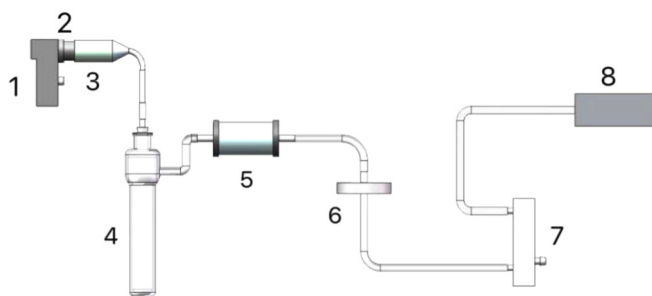


FIG. 2. Schematic of experimental setup (1: VMN, 2: silicone mouthpiece, 3: idealized MT airway model, 4: bubble absorption tube, 5: prefilter, 6: membrane filter, 7: glass rotor flowmeter, and 8: vacuum pump).

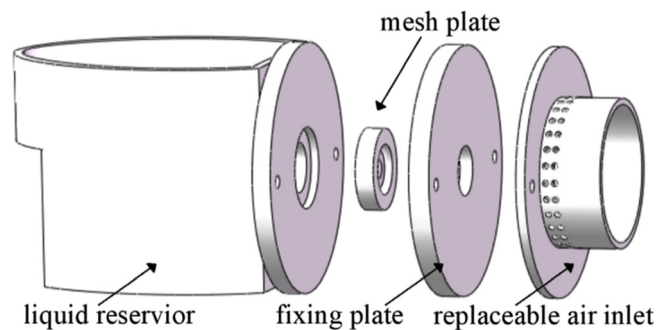


FIG. 3. Assembly schematic of the VMN body and the mesh plate.

The idealized MT model proposed by Zhang *et al.*⁴³ was capable of replicating the deposition characteristics of inhaled particulate matter in human MT airways. This idealized MT model has an inlet diameter of 3 cm, gradually narrowing to a 0.85 cm diameter tube at the oropharyngeal region and then bending 90° downward at the level of the pharynx to enter the throat region. The left side of Fig. 4 illustrates the idealized MT airway model used in this study, while the right side displays a sagittal head CT image of an adult male, with labels indicating the regions of the oral cavity, oropharynx, and throat in both the MT model and the CT image. The model was sectioned along the sagittal plane, facilitating the visualization and analysis of the inner surface. To ensure the surface smoothness, the Computer Numerical Control (CNC)-manufactured aluminum MT airway model was analyzed.

Before each experiment, the bubble absorption tube was filled with de-ionized water (Nandye Co., Ltd., Wenzhou, Zhejiang, China). This tube served as a micro-liquid-gas bubbling bed, capturing most droplets that escaped from the MT airway model. To intercept large droplets that might be generated by the breakage of bubbles inside the bubble absorption tube, a prefilter was employed. All remaining small droplets were collected using a membrane filter with a pore size of $0.1\ \mu\text{m}$ (Yaxin Co., Ltd., Shanghai, China).

B. Experimental overview

For each test, the experimental system shown in Fig. 2 was utilized. The flow rate was adjusted by the glass rotor flowmeter. Subsequently, a water solution consisting of 0.9% w/v NaCl and 0.1% w/v fluorescein sodium was nebulized using a VMN. It should be noted that the actual drug solution is micrograms or milligrams of drug dissolved in normal saline (0.9% w/v NaCl water solution). The nebulized droplets were carried along by the airflow, with a portion of them depositing within the idealized MT airway model. Meanwhile, the remaining droplets escaped from the airway model and were collected using a bubble absorption tube, prefilter, and membrane filter. To maintain the integrity of the experiment and prevent filter overload, each individual test lasted between 3 and 5 min. This duration also ensured that no droplets coalesced and slid down within the MT model during the experiment.

After each deposition test, the airway model was detached from the system and disassembled to expose the inner surface for deposition pattern photography (see Sec. II C for details). The weight of the VMN was measured before and after the experiment to determine the mass

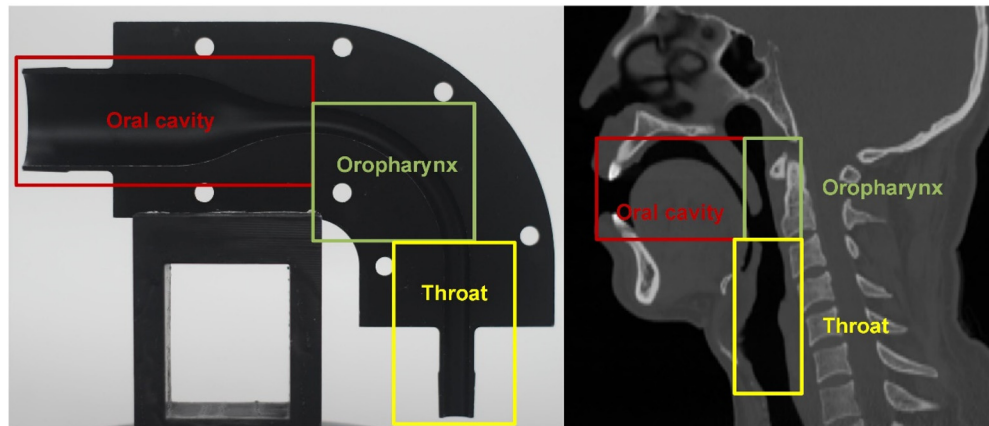


FIG. 4. Idealized MT model and human CT image with labeled oral cavity, oropharynx, and throat.

of the nebulized solution. The mouthpiece, airway model, bubble absorption tube, prefilter, membrane filter, and tubes connecting these components were rinsed in ultrasonic cleaner (Huace Science and Technology Co., Ltd., Shenzhen, Guangdong, China). The rinsate of different components was brought to a fixed volume separately. Then, the concentration of the rinsate was measured to determine the amount of deposited droplets in each component. Two concentration measurement methods, i.e., visible light spectrophotometry and fluorescence spectrophotometry, were used to measure the concentration of the rinsate, and it was found that they were equivalent.

The droplet nebulization and deposition tests using VMN1 and VMN2 were conducted at inhalation flow rates of 15, 22.5, 30, 45, and 60 l/min. To ensure reliable results, each experimental condition was repeated three times, resulting in triplicate measurements for each flow rate.

C. Nebulization characteristics of VMNs

The nebulization mass flow rates of VMN1 and VMN2 are 0.35 and 0.23 g/min, respectively. Figure 5 shows the droplet size distributions of the aerosol generated by the two VMNs. The droplet size distribution was obtained by averaging ten measurements from a high-speed particle size analyzer (Spraylink, Zhuhai Linkoptic Instrument Co. LTD, Guangdong, China) over a period of 10 s. For VMN1, the calculated MMAD (Mass Median Aerodynamic Diameter) is $4.40\ \mu\text{m}$, and the GSD (Geometric Standard Deviation) is 1.73. On the other hand, for VMN2, the MMAD is $3.48\ \mu\text{m}$, and the GSD is 1.47. Notably, despite using the same driver, VMN2, which has more orifices, exhibits a lower nebulization mass flow rate and smaller MMAD. This may be attributed to the vibration characteristics of the vibrating plate.

D. Measurement of deposition patterns

The experimental setup for measuring the deposition pattern is illustrated in Fig. 6. It comprised several components, including a camera, two ultraviolet (UV) lamps equipped with diffusers, the MT model, a black absorbent background, and a support structure for the MT model. The UV lamps emitted light that could excite the fluorescent substance in the droplets, causing them to emit fluorescence. Compared to visible light sources, the invisible UV light minimized

the entry of visible light into the camera lens through reflection, thus enhancing the contrast of local fluorescence. The main spectral radiation of UV lamp is concentrated in the range of 200–280 nm, with a small amount of blue light emission to indicate the proper functioning of the lamp. A single-lens reflex camera (EOS 600D, Canon, Inc., Kaohsiung, China) was employed to capture the fluorescent droplet deposition pattern. The black absorbent background was used to reduce the reflection of light into the camera lens. The support structure, 3D printed, held half of the MT model vertically, providing a clear display of the inner surface of the MT model. Throughout all measurements, the relative positions of various components remained unchanged.

E. Analysis of deposition fraction

The deposition fraction (DF) is defined as

$$DF = \frac{m_1}{m_1 + m_2} \times 100\%, \quad (1)$$

where m_1 represents the mass of NaCl droplets deposited in the mouthpiece and MT model, and m_2 represents the mass of NaCl droplets escaped from the MT model. m_2 includes the mass of NaCl droplets captured by the bubble absorption tube, prefilter, membrane filter, and tubes connecting these components.

In this experiment, the rinsate was a low-concentration fluorescent NaCl solution. Typically, the concentration of fluorescent solutions is measured using fluorescence spectrophotometry, which is a common method. However, it is worth noting that different concentrations of NaCl solutions exhibit varying absorbance characteristics, and in principle, they can also be measured using visible spectrophotometry. Hence, this study aimed to investigate the equivalence of these two methods by comparing their results.

The fluorescent solution was diluted to different levels to prepare sample solutions with fluorescein concentrations of 0.00004, 0.0001, 0.0002, and 0.0005 g/l, respectively. Additionally, a solution with a fluorescein concentration of 0.00004 g/l was prepared to assess the accuracy of the fluorescence spectrophotometer (FluoroMax-4, HORIBA (China) Trading Co., Ltd., Shanghai, China) and visible spectrophotometer [722G, INESA (Group) Co., Ltd., Shanghai, China].

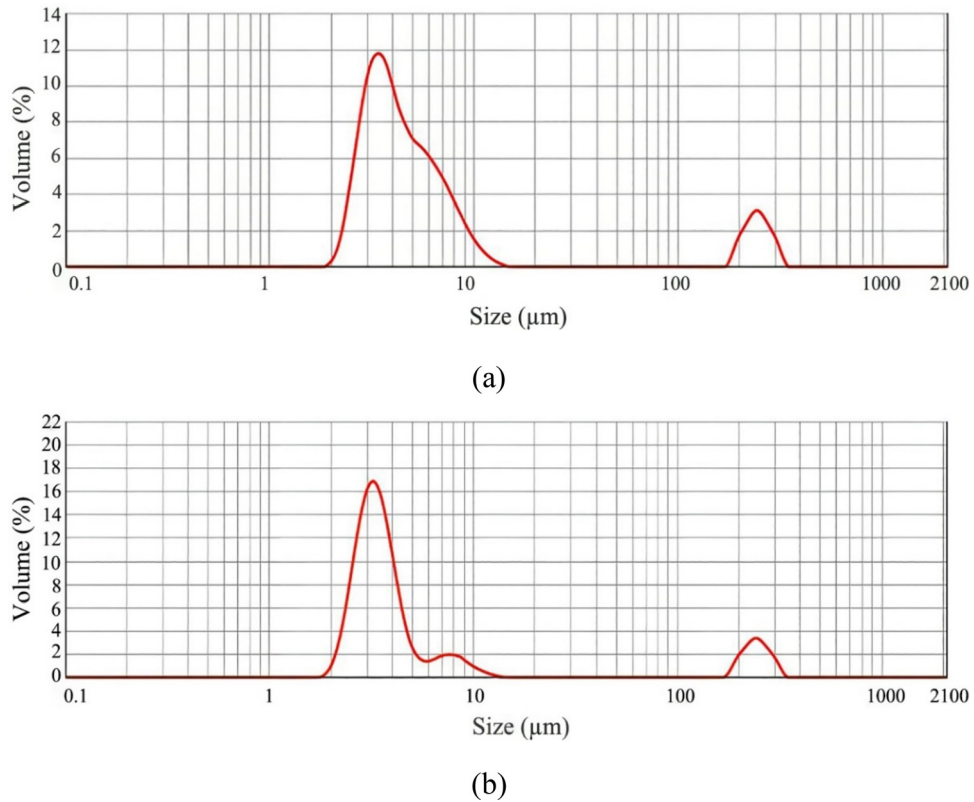


FIG. 5. Droplet size distributions for different VMNs: (a) VMN1 and (b) VMN2.

Under the specific condition of an inhalation flow rate equal to 30l/min, the rinsate was subjected to concentration measurement using both fluorescence spectrophotometry and visible spectrophotometry to determine the deposition fraction. The weight change of the nebulizer before and after the experiment was 0.432 g. It indicated that 0.432 g of the solution was nebulized, corresponding to a mass of 4.32×10^{-4} g of fluorescein.

To ensure accuracy and reliability, all measurements were repeated three times.

1. Fluorescence spectrophotometry

When the concentration of the fluorescent solution is low, the fluorescence intensity F (a.u.) of the solution is linearly related to the

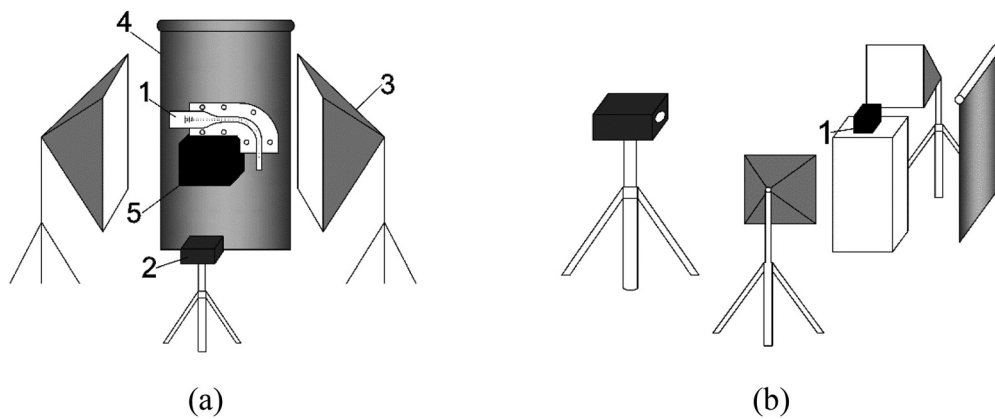


FIG. 6. Schematic of photographing setup (1: MT model, 2: camera, 3: UV lamp with diffuser, 4: black absorbent background, and 5: model support): (a) anterior view and (b) side view.

20 August 2023 14:29:04

concentration C (g/l) of the fluorescent substance in the solution.^{44,45} By measuring the sample solutions on the fluorescence spectrophotometer, the following relationship was obtained: $F = 5.81 \times 10^9 C + 74623.84$. Based on this relationship, the fluorescence intensity of the sample with a concentration of 0.00004 g/l was measured to be 289650.17 (a.u.), corresponding to a concentration of 0.000037 g/l. The measurement error was calculated to be 7.5%.

For the inhalation flow rate of 30 l/min, the mass of fluorescein deposited in the MT model was measured to be 7.590×10^{-5} g, while the mass of fluorescein escaping from the model's outlet was 3.241×10^{-4} g. Therefore, the total mass of fluorescein measured was 4.000×10^{-4} g, resulting in a deposition fraction of 18.97%. The relative error in the mass of the nebulized solution was 7.41%.

2. Visible spectrophotometry

According to the Beer–Lambert law,^{46,47} the relationship between absorbance A (l/g cm) and fluorescein concentration C (g/l) was obtained by testing the four sample solutions, which is given as $A = 45.27C + 1.77 \times 10^{-4}$. According to this relationship, the concentration of the sample with a fluorescence substance concentration of 0.00004 g/l was measured as 0.0000403 g/l, with a measurement error of 0.75%.

For the rinsate under the inhalation flow rate of 30 l/min, the deposited mass of fluorescein in the MT model was 8.125×10^{-5} g, while the escaped mass from the outlet of the model was 3.375×10^{-4} g, resulting in a deposition fraction of 19.40%. The total mass of aerosolized fluorescein was 4.1875×10^{-4} g, with a relative error of 3.07% compared to the actual total mass aerosolized.

While fluorescence spectrophotometry is a widely used method for measuring the concentration of fluorescent solutions, it is important to note that visible spectrophotometry showed consistent accuracy compared to fluorescence spectrophotometry for the NaCl and fluorescent aqueous solution utilized in this experiment. As a result, visible spectrophotometry was selected as the preferred method for measuring the deposition fraction of nebulized droplets in the subsequent experiments.

III. RESULTS AND DISCUSSION

A. Deposition fraction (DF)

Figure 7(a) presents the variation of nebulized droplet deposition in the idealized MT airway model concerning inspiratory flow rate. Figure 7(b) illustrates the DFs as a function of the corresponding inertial parameter (IP), defined as

$$IP = \rho_d d_d^2 Q, \tag{2}$$

where ρ_d (g/cm³) is the droplet density, d_d (μ m) is the MMAD of the droplet, and Q (cm³/s) is the inhalation flow rate. The discrete data points in Figs. 7(a) and 7(b) represent the average values obtained from of three repeats. The error bars accompanying the data points indicate the standard deviation.

The DF curves for VMN1 and VMN2 in Fig. 7 show a decreasing trend, followed by an increasing trend as the flow rate increases. The observed difference in the results, where the deposition fraction curves in our study exhibit a non-monotonic trend with the increase in the flow rate, contrasts with the findings of Zhang *et al.*,⁴⁸ who reported a consistent increase in the deposition fraction with increasing IP using di-ethylhexyl sebacate (DEHS) droplets.

The observed difference in the deposition fraction between the saline solution and DEHS droplets can be attributed to several factors. In our experiment, the use of saline solution leads to evaporation in the air, which can affect the behavior of the droplets. In contrast, DEHS droplets are more stable and do not evaporate or absorb moisture from the air. Consequently, the deposition fraction of DEHS droplets tends to increase as droplet inertia increases, which can be achieved by increasing the droplet diameter or the inhalation flow rate.

In the case of the VMN employed in our experiment, the aerosol mass flow rate remains constant. Therefore, as the inhalation flow rate increases, the droplets are diluted in a larger air volume. Previous experiments have shown that a NaCl solution has a threshold relative humidity (RH) of approximately 76%.⁴⁹ Specifically, below this threshold (RH = 76%), the solution will continuously evaporate, and NaCl crystals will form through crystallization. Therefore, at higher ambient RH levels, NaCl droplets may interact with the environment through water vapor exchange and eventually reach an equilibrium state. The

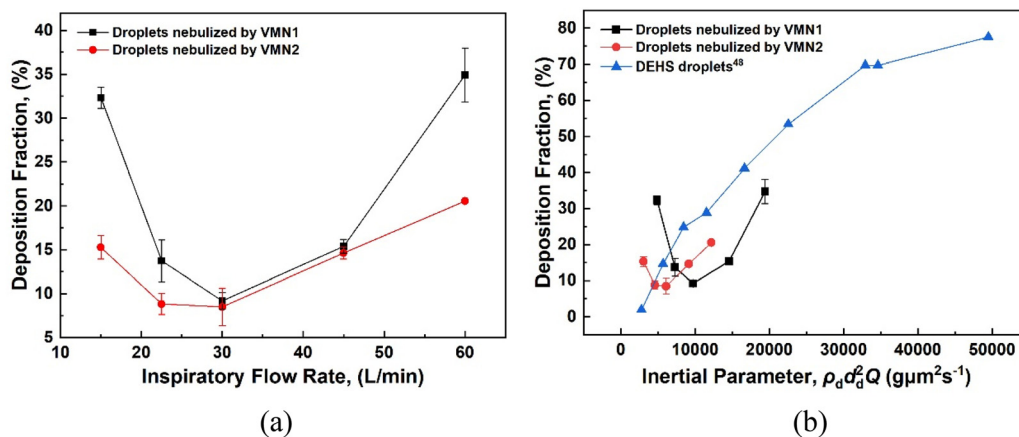


FIG. 7. Droplet DFs in the idealized MT airway: (a) variations with inspiratory flow rate and (b) variations with inertial parameter.

droplet–water vapor interaction model can be referred to from previous research results.^{50–52} Based on the model validation in our numerical simulations, the model can accurately describe the hygroscopic growth processes of NaCl particles and glycerol droplets.⁵² This model assumes the presence of an extremely thin air layer on the surface of the droplets, with the mass fraction of the evaporable component in this thin layer determined by the modified Raoult's law.⁵³ This enables the calculation of mass exchange occurring between the droplet and the surrounding air. Consequently, the equilibrium RH of pure water droplets is 100%. However, when the droplets contain soluble components, the mass fraction of water in the droplets decreases, leading to a corresponding decrease in the equilibrium RH. In the case of water droplets containing soluble components, if the environmental RH drops below a critical threshold, the droplets will undergo crystallization and continue to evaporate until only solid particles remain.

This behavior explains the differences in the deposition fraction between the saline solution and DEHS droplets. As the saline solution droplets interact with the environment, undergoing evaporation and potential crystallization, the deposition fraction trends differ from the more stable and non-evaporating DEHS droplets.

Although the temperature and humidity conditions were controlled during the deposition experiments, non-uniformity would occur in the processes of nebulization, droplet transport, and evaporation within the MT model. The current experimental setup is unable to describe the non-uniform humidity distribution. Therefore, for theoretical analysis, we assume an idealized uniform droplet evaporation process. Assuming that the physiologic saline aerosol is uniformly distributed in the inhaled air, and all droplets evaporate into saturated saline (corresponding to an equilibrium RH of 76%), the air humidity under different inhalation flow rates of 15, 22.5, 30, 45, and 60 l/min for VMN1 will reach 140.7%, 110.5%, 95.4%, 80.3%, and 72.7%, respectively. Similarly, for VMN2, the corresponding air humidities will be 109.6%, 89.7%, 79.8%, 69.9%, and 64.9% under the same inhalation flow rates.

Under the predicted conditions of VMN1 at 60 l/min and VMN2 at 45 and 60 l/min, the ambient air relative humidity (RH) falls below the critical threshold of 76%, indicating that the droplets will continue to evaporate, resulting in crystal precipitation. Even if we assume that the 0.35 g/min aerosol generated by VMN1 and the 0.23 g/min aerosol generated by VMN2 are composed of pure water and completely evaporate, the resulting increase in ambient air RH would only be 73.2%, 70.4%, and 65.3%, respectively, for VMN1 at 60 l/min, VMN2 at 45 l/min, and VMN2 at 60 l/min conditions. Therefore, it is likely that the droplets in these scenarios will fully evaporate during the transport process. For the other conditions, the droplets may reach an equilibrium state with the ambient air between the predicted ambient RH and 76%. However, it is essential to note that in the actual experimental process, the distribution of droplets in the MT model is non-uniform, leading to regions with varying RH values. To provide a more detailed analysis, computational fluid–particle dynamics (CFPD) are required, involving two-way coupled mass transfer between the continuous and discrete phases.

Based on the estimated evaporation of droplets and changes in RH of the inhaled air, we can explain the variations in nebulized droplet DF in the MT model. At an inhalation flow rate of 15 l/min, droplet evaporation is suppressed, resulting in larger droplet diameters and higher inertia. Gravity settling has a more pronounced effect at lower

inhalation flow rates, leading to higher deposition fractions. VMN1, with its higher nebulization rate and MMAD, exhibits a higher deposition fraction of 32.36%, whereas VMN2 has a lower deposition fraction of 15.25%. As the inhalation flow rate gradually increases to 30 l/min, droplet evaporation becomes more complete, and the droplet diameter decreases. This allows the droplets to follow the airflow more effectively and exit the MT model, resulting in gradual decreases in deposition fractions for both VMN1 and VMN2. At this point, the deposition fractions for VMN1 and VMN2 decrease to 9.22% and 8.49%, respectively. When the inhalation flow rate further increases to 60 l/min, the droplets can almost completely evaporate into particles. Although the particle mass remains nearly constant, the increased velocity leads to higher inertia and, consequently, higher deposition fractions. The deposition fractions for VMN1 and VMN2 gradually increase to 34.72% and 20.57%, respectively. Considering that the typical inhalation flow rate during rest is around 15 l/min, the flow rate during drug administration may be even lower. Therefore, to improve pulmonary drug delivery efficiency within an acceptable nebulization time, a lower nebulization rate similar to VMN2 can be advantageous.

The experimental results discussed earlier can provide valuable insight for optimizing the operating parameters of nebulizers and enhancing the efficiency of pulmonary drug or vaccine delivery, with a particular focus on mesh nebulizers. These nebulizers typically have a current mass median aerodynamic diameter (MMAD) between 4 and 5 μm . To achieve optimal pulmonary delivery efficiency of inhaled drugs or vaccines, several factors should be considered.

First, controlling the temperature and humidity of the inhaled air is crucial as it affects droplet evaporation and influences droplet size. Achieving appropriate conditions for droplet evaporation can lead to a reduction in the droplet size to the desired range of 1–3 μm . This size range is advantageous for minimizing deposition in the oropharyngeal region and enhancing lung delivery efficiency. Previous experiments have shown that the deposition fraction of droplets generated by the nebulizer in the idealized MT model is influenced by the ambient temperature and humidity. It has been observed that in high-temperature and high-humidity environments, the deposition fraction is higher compared to indoor environments.²⁴

The composition and dosage of the drug or vaccine should also be carefully considered, as different substances may have varying evaporation characteristics and optimal droplet sizes for effective delivery. Furthermore, understanding the inhalation flow rate of the users is crucial for optimizing delivery. Fine-tuning parameters, such as nebulization rate, droplet size, and inhalation technique to match the preferred inhalation flow rate can ensure efficient drug or vaccine delivery.

In addition to these considerations, it is crucial to account for the realistic temperature and humidity conditions of the human airway during nebulizer optimization. The human respiratory tract has a higher temperature than the ambient air, and the presence of a mucous layer on the respiratory tract surface leads to humidification and heating of the inhaled air. As a result, the degree of evaporation of droplets in the extrathoracic airway will be reduced compared to the experimental results presented here. Therefore, when optimizing the nebulizer's output for a certain inspiratory flow rate, it is necessary to further reduce the nebulization rate based on the considerations of realistic airway conditions. To achieve a more detailed and quantitative analysis, numerical simulations might be required, which consider the

airflow dynamics and heat and mass transfer phenomena at the boundaries of the real respiratory tract geometry.

By considering and optimizing factors, such as temperature, humidity, drug formulation, dosage, and inhalation flow rate, it is possible to enhance the pulmonary delivery efficiency of inhaled drugs or vaccines. These optimizations can lead to improved therapeutic outcomes and better patient experiences.

B. Deposition pattern

Figure 8 visualizes the deposition patterns of VMN1 and VMN2 in the idealized MT model at different inhalation flow rates. It should be noted that to prevent coalescence and droplet dripping from the model, the experimental durations varied slightly for different inhalation flow rates. Consequently, the deposition patterns within each sub-figure can describe the locations of droplet deposition and the relative

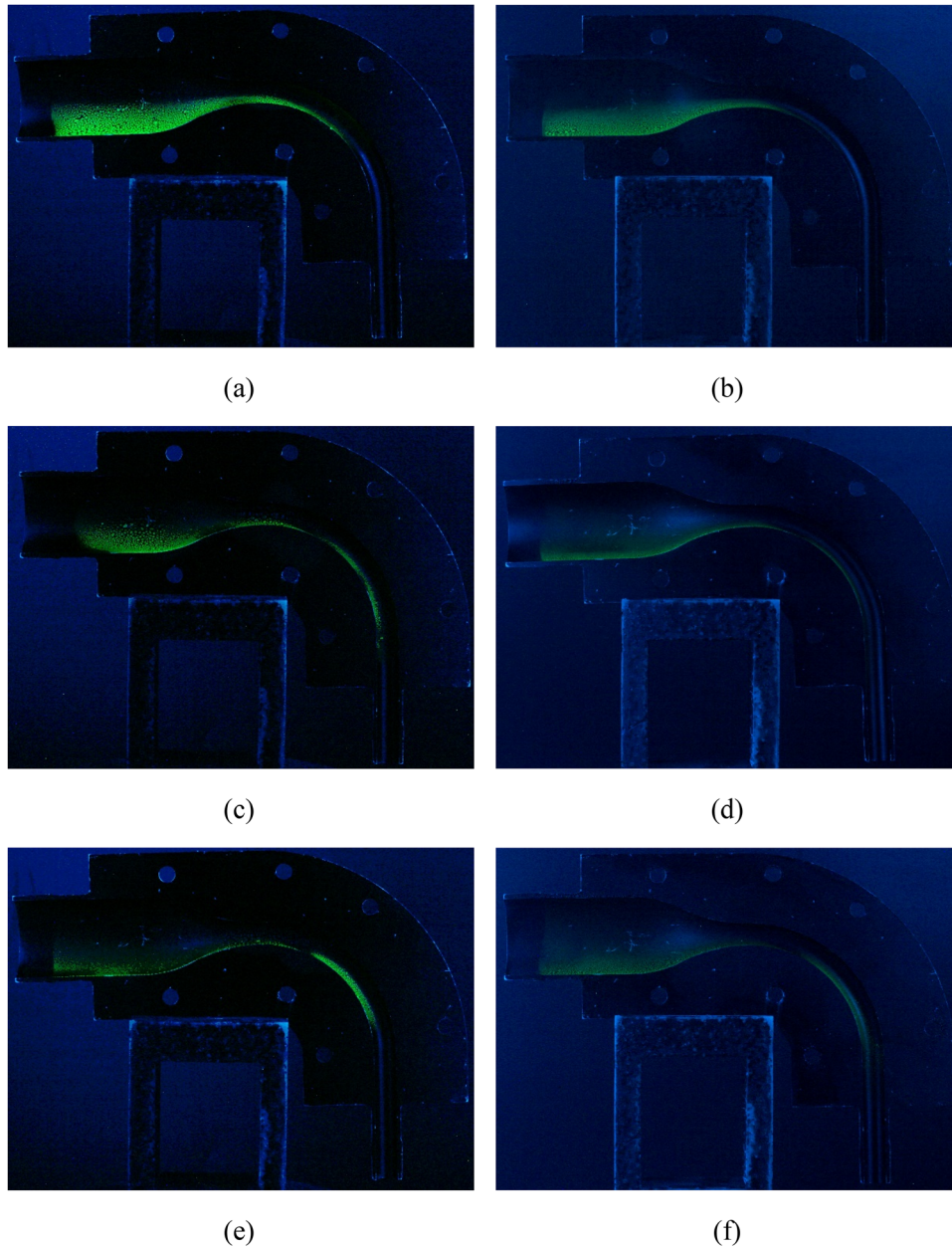


FIG. 8. Deposition patterns of nebulized droplets in an idealized MT model at different inhalation flow rates: (a) VMN1 at 15 l/min; (b) VMN2 at 15 l/min; (c) VMN1 at 22.5 l/min; (d) VMN2 at 22.5 l/min; (e) VMN1 at 30 l/min; (f) VMN2 at 30 l/min; (g) VMN1 at 45 l/min; (h) VMN2 at 45 l/min; (i) VMN1 at 60 l/min; and (j) VMN2 at 60 l/min.

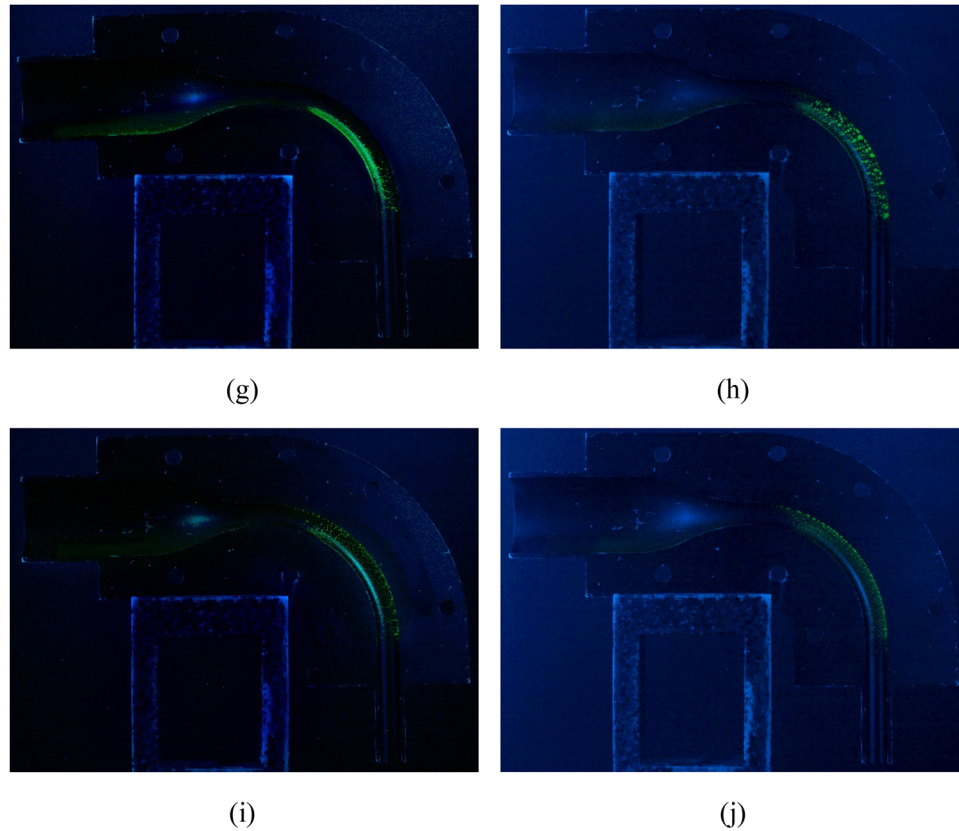


FIG. 8. (Continued.)

deposition amounts under their respective operating conditions, with brighter fluorescence indicating higher deposition amounts. However, it is currently challenging to compare the absolute deposited droplet mass between the different subfigures.

Overall, the deposition patterns of VMN1 and VMN2 are similar, with slight variations observed at each flow rate. Under the 15 l/min inhalation condition, there are substantial and relatively uniform depositions of droplets in the middle and lower regions of the oral cavity [see Figs. 8(a) and 8(b)]. This observation suggests that the droplets are relatively large and are primarily influenced by gravitational sedimentation and secondary flows, causing them to disperse, settle, and deposit at the bottom part of the oral cavity. Additionally, some deposited droplets are observed in locations extending from the oral cavity to the anterior side of the oropharynx [see Fig. 8(a)]. However, VMN2, with a smaller nebulization rate and MMAD, exhibits a slightly different deposition pattern. As illustrated in Fig. 8(b), reduced deposition is observed outside the oral cavity, indicating that the droplets might efficiently follow the lower velocity airflow and exited the MT model after passing through the oral cavity.

When the inhalation flow rate is increased to 22.5 l/min, droplet deposition in the oral cavity starts to decrease, gradually extending toward the anterior side of the oropharynx. There is less deposition of droplets generated by VMN2 in the anterior oropharynx [see Fig. 8(d)], while the deposition area of VMN1 expands to the vertical segment of the pharynx [see Fig. 8(c)]. When the inspiratory flow rate is

further increased to 30 l/min [see Fig. 8(f)], an increased deposition of droplets can be observed in the anterior oropharynx. The deposition area expands circumferentially due to the influence of secondary flow,⁵⁴ occupying approximately half of the circumference of the oropharynx. For VMN1 [see Fig. 8(e)], the deposition of droplets in this region is even more pronounced, with higher fluorescence intensity compared to the oral cavity region.

Figures 8(g) and 8(h) present the deposition patterns of fluorescent droplets at an inspiratory flow rate of 45 l/min. There is a significant reduction in deposition within the oral cavity, with only a small amount of deposition observed at the bottom. A large number of droplets deposited in the oropharyngeal region, covering almost the entire circumference. This is depicted in Figs. 8(i) and 8(j). The results indicate that as the inspiratory flow rate increases, the distribution of deposited droplets shifts from the oral cavity toward the oropharynx and larynx, highlighting the importance of flow dynamics in determining the deposition patterns of inhaled droplets.

However, it is important to acknowledge that the measured deposition patterns in our experiment may differ significantly from the droplet transport and deposition results obtained from one-way coupled Euler–Lagrange simulations.^{55,56} The one-way coupled Euler–Lagrange simulation results are unable to capture the influence of droplet evaporation on the humidity of the inhaled air, thereby incapable of predicting the scenario where droplets reach equilibrium and further evaporation is inhibited due to increased environmental

humidity. Although it is technically feasible to modify the computational model and include two-way coupling between the Eulerian phase (airflow) and Lagrangian phase (individual droplets), simulating the movement, evaporation, and deposition of a large number of individual droplets, as observed in this experiment, presents significant computational challenges. For example, assuming a nebulization volume rate of 0.22 ml/min and droplets with an average size of 5 μm , approximately 50×10^6 droplets would be nebulized per second. The computational complexity and memory requirements would escalate significantly, rendering such a simulation infeasible within reasonable time constraints.

The idealized MT model used in this study can mimic total deposition in the extrathoracic region. However, it is essential to acknowledge that the deposition locations of droplets within this idealized model may differ from those in the actual respiratory airways due to the model's simplified internal structure, which reduces the complexity of airflow. To gain a comprehensive understanding of aerosol deposition in the human respiratory system, it is necessary to conduct further experimental and numerical studies that investigate the deposition of aerosol droplets in the actual human respiratory airways.

Nevertheless, the experimental results, including deposition fractions and deposition patterns of nebulized droplets, serve as reliable validation data for numerical simulation studies. Building upon this validated model, numerical simulations can further consider the influence of warm and humid airway boundaries and the complexities of respiratory tract geometry. By incorporating these factors, we can enhance the predictive capabilities of numerical simulations in simulating the actual process of nebulized drug delivery under realistic respiratory conditions.

By visually observing the deposition locations of droplets, this experimental method can be applied to the optimization of inhalation devices. It allows for quick identification of specific structural features that may need fine-tuning to enhance the deposition fraction in targeted areas. Furthermore, this experimental method also has the potential to be extended to *in vitro* experiments with exhaled aerosols, enabling the assessment of exposure risks in different scenarios.

IV. CONCLUSIONS

In this study, we conducted deposition experiments of nebulized droplets in an idealized MT airway model using custom VMNs. These experiments were performed at five flow rates ranging from 15 to 60 l/min, employing two VMNs. A novel method was proposed to measure the deposition fractions and deposition patterns of the nebulized droplets simultaneously. To our knowledge, this method represents a pioneering experimental approach that enables simultaneous acquisition of regional and local deposition information. Based on the experimental results, the following conclusions were drawn:

1. The utilization of a normal saline solution containing fluorescein as the nebulization solution enabled visualization of the deposition patterns in the airway model under UV light. By measuring the fluorescence intensity or absorbance of the rinsate from each experimental component, we accurately obtained both the deposition pattern and deposition fraction of nebulized droplets within a single experiment.
2. Both VMN1 and VMN2, which have the same structure but different numbers of orifices, exhibited a decrease, followed by an

increase in the deposition fraction with increasing inspiratory flow rate.

3. VMN1 with 1200 orifices had a lower nebulization rate, MMAD, and DF compared to VMN2 with 700 orifices. This indicates that within an appropriate nebulization time, a lower nebulization rate can improve the pulmonary drug delivery efficiency.
4. With the increment of inspiratory flow rate, the deposition of aerosol droplets shifted from the oral region of the idealized MT model to the pharyngeal region.

ACKNOWLEDGMENTS

The authors gratefully acknowledge the financial support of the National Natural Science Foundation of China (Grant No. 51976091) and Qinglan Project of Jiangsu Province.

AUTHOR DECLARATIONS

Conflict of Interest

The authors have no conflicts to disclose.

Author Contributions

Xiaole Chen: Formal analysis (equal); Methodology (lead); Project administration (lead); Writing – review & editing (equal). **Yi Jin:** Data curation (equal); Formal analysis (equal); Investigation (equal); Writing – original draft (lead). **Yu Feng:** Formal analysis (equal); Investigation (equal); Writing – review & editing (equal). **Zhenning Jia:** Resources (lead). **Jinan Zhang:** Data curation (equal); Visualization (lead). **Xiaojuan Xie:** Resources (supporting). **Ya Zhang:** Resources (supporting).

DATA AVAILABILITY

The data that support the findings of this study are available from the corresponding author upon reasonable request.

REFERENCES

- ¹M. Singh, A. G. Duarte, E.-S. Hsu, Y.-F. Kuo, and G. Sharma, "Trends and factors associated with nebulized therapy prescription in older adults with chronic obstructive pulmonary disease from 2008 to 2015," *J. Aerosol Med. Pulm. Drug Delivery* **33**, 161–169 (2020).
- ²M. Cazzola, J. Ora, L. Calzetta, P. Rogliani, and M. G. Matera, "The future of inhalation therapy in chronic obstructive pulmonary disease," *Curr. Res. Pharmacol. Drug Discovery* **3**, 100092 (2022).
- ³D. P. Tashkin, "A review of nebulized drug delivery in COPD," *Int. J. Chronic Obstruct. Pulm. Dis.* **11**, 2585–2596 (2016).
- ⁴Z. Zhu, J. Zheng, Z. Wu, Y. Xie, Y. Gao, L. Zhong, and M. Jiang, "Clinical practice of nebulized therapy in China: A national questionnaire survey," *J. Aerosol Med. Pulm. Drug Delivery* **27**, 386–391 (2014).
- ⁵V. Forest and J. Pourchez, "Nano-delivery to the lung- by inhalation or other routes and why nano when micro is largely sufficient?," *Adv. Drug Delivery Rev.* **183**, 114173 (2022).
- ⁶S. Hou, J. Wu, X. Li, and H. Shu, "Practical, regulatory and clinical considerations for development of inhalation drug products," *Asian J. Pharm. Sci.* **10**, 490–500 (2015).
- ⁷L. Fromer, E. Goodwin, and J. Walsh, "Customizing inhaled therapy to meet the needs of COPD patients," *Postgrad. Med.* **122**, 83–93 (2010).
- ⁸J. N. Pritchard, R. H. M. Hatley, J. Denyer, and D. von Hollen, "Mesh nebulizers have become the first choice for new nebulized pharmaceutical drug developments," *Ther. Delivery* **9**, 121–136 (2018).

- ⁹Y. S. Adachi, T. Itazawa, M. Nakabayashi, T. Fuchizawa, Y. Okabe, Y. Ito, Y. Adachi, G. Murakami, and T. Miyawaki, "Safety and usefulness of a novel eMotion electric mesh nebulizer in children with asthma," *Allergol. Int.* **55**, 167–171 (2006).
- ¹⁰R. Dhand, "Nebulizers that use a vibrating mesh or plate with multiple apertures to generate aerosol," *Respir. Care* **47**, 1406–1416 (2002).
- ¹¹J. S. Lass, A. Sant, and M. Knoch, "New advances in aerosolised drug delivery: Vibrating membrane nebuliser technology," *Expert Opin. Drug Delivery* **3**, 693–702 (2006).
- ¹²K. H. Chang, B. J. Park, and K. C. Nam, "Aerosolization performance of immunoglobulin G by jet and mesh nebulizers," *AAPS PharmSciTech* **24**, 125 (2023).
- ¹³W. H. Finlay, *The Mechanics of Inhaled Pharmaceutical Aerosols*, 2nd ed. (Academic Press, 2019).
- ¹⁴B. Vukasinovic, M. K. Smith, and A. Glezer, "Spray characterization during vibration-induced drop atomization," *Phys. Fluids* **16**, 306–316 (2004).
- ¹⁵Y. Wang and R. E. Khayat, "The effects of gravity and surface tension on the circular hydraulic jump for low- and high-viscosity liquids: A numerical investigation," *Phys. Fluids* **33**, 012105 (2021).
- ¹⁶N. J. Cira, A. Benusiglio, and M. Prakash, "Dancing droplets: Autonomous surface tension-driven droplet motion," *Phys. Fluids* **26**, 091113 (2014).
- ¹⁷N. Pandurangan and S. Sahu, "Spatial evolution of multi-scale droplet clusters in an evaporating spray," *Phys. Fluids* **34**, 113310 (2022).
- ¹⁸X. A. Si, M. Talaat, and J. Xi, "SARS COV-2 virus-laden droplets coughed from deep lungs: Numerical quantification in a single-path whole respiratory tract geometry," *Phys. Fluids* **33**, 023306 (2021).
- ¹⁹A. K. Mallik, S. Mukherjee, and M. V. Panchagnula, "An experimental study of respiratory aerosol transport in phantom lung bronchioles," *Phys. Fluids* **32**, 111903 (2020).
- ²⁰J. Choi, M. H. Tawhai, E. A. Hoffman, and C.-L. Lin, "On intra- and intersubject variabilities of airflow in the human lungs," *Phys. Fluids* **21**, 101901 (2009).
- ²¹G. Zeng, L. Chen, H. Yuan, A. Yamamoto, and S. Maruyama, "Evaporation flow characteristics of airborne sputum droplets with solid fraction: Effects of humidity field evolutions," *Phys. Fluids* **33**, 123308 (2021).
- ²²J. Dugernier, M. Hesse, R. Vanbever, V. Depoortere, J. Roeseler, J.-B. Michotte, P.-F. Laterre, F. Jamar, and G. Reyckler, "SPECT-CT comparison of lung deposition using a system combining a vibrating-mesh nebulizer with a valved holding chamber and a conventional jet nebulizer: A randomized cross-over study," *Pharm. Res.* **34**, 290–300 (2017).
- ²³J. C. Waldrep and R. Dhand, "Advanced nebulizer designs employing vibrating mesh/aperture plate technologies for aerosol generation," *Curr. Drug Delivery* **5**, 114–119 (2008).
- ²⁴H. Yang, Y. Wang, X. Chen, B. Sun, F. Tao, X. Xie, and Y. Zhang, "The effects of temperature and humidity on the deposition of nebulized droplet in an idealized mouth-throat model," *Flow Meas. Instrum.* **91**, 102359 (2023).
- ²⁵H. M. Park, K. H. Chang, S.-H. Moon, B. J. Park, S. K. Yoo, and K. C. Nam, "In vitro delivery efficiencies of nebulizers for different breathing patterns," *BioMed. Eng. Online* **20**, 59 (2021).
- ²⁶S. Gürzing, A. L. Thiebes, C. G. Cornelissen, S. Jockenhoevel, and M. A. Reddemann, "Suitability of bronchoscopic spraying for fluid deposition in lower airway regions: Fluorescence analysis on a transparent in vitro airway model," *J. Aerosol Med. Pulm. Drug Delivery* **35**, 269–277 (2022).
- ²⁷X. Xia, T. Ding, X. Chen, F. Tao, B. Sun, T. Lu, J. Wang, Y. Huang, and Y. Xu, "Evaporation affects the in vitro deposition of nebulized droplet in an idealized mouth-throat model," *Atmosphere* **14**, 93 (2023).
- ²⁸B. Grgic, W. H. Finlay, and A. F. Heenan, "Regional aerosol deposition and flow measurements in an idealized mouth and throat," *J. Aerosol Sci.* **35**, 21–32 (2004).
- ²⁹W. C. Su and Y. S. Cheng, "Fiber deposition pattern in two human respiratory tract replicas," *Inhalation Toxicol.* **18**, 749–760 (2006).
- ³⁰H. Sakai, Y. Watanabe, T. Sera, H. Yokota, and G. Tanaka, "Visualization of particle deposition in human nasal cavities," *J. Visualization* **18**, 349–357 (2015).
- ³¹S. Sahu, A. Chakraborty, and D. Maurya, "Coriolis-induced liquid breakup and spray evolution in a rotary slinger atomizer: Experiments and analysis," *Int. J. Multiphase Flow* **135**, 103532 (2021).
- ³²A. Chakraborty, S. Sahu, and D. Maurya, "Effect of orifice size on liquid breakup dynamics and spray characteristics in slinger atomizers," *Proc. Inst. Mech. Eng., Part A* **236**, 1158–1170 (2022).
- ³³A. Chakraborty, M. Das, S. Sahu, and D. Maurya, "A parametric study on rotary slinger spray characteristics using laser diagnostics," in *Proceedings of the National Aerospace Propulsion Conference* (Springer Nature Singapore, Singapore, 2023); available at https://link.springer.com/chapter/10.1007/978-981-19-2378-4_36
- ³⁴J. X. Xi, T. C. Yang, K. Talaat, T. S. Wen, Y. Zhang, S. Klozik, and S. Peters, "Visualization of local deposition of nebulized aerosols in a human upper respiratory tract model," *J. Visualization* **21**, 225–237 (2018).
- ³⁵L. Liu, Y. Li, P. V. Nielsen, J. Wei, and R. L. Jensen, "Short-range airborne transmission of expiratory droplets between two people," *Indoor Air* **27**, 452–462 (2017).
- ³⁶J. Yang, S. C. Sekhar, K. W. D. Cheong, and B. Raphael, "Performance evaluation of a novel personalized ventilation-personalized exhaust system for airborne infection control," *Indoor Air* **25**, 176–187 (2015).
- ³⁷S. Liu and A. Novoselac, "Transport of airborne particles from an unobstructed cough jet," *Aerosol Sci. Technol.* **48**, 1183–1194 (2014).
- ³⁸X. Li, C. M. Mak, K. W. Ma, and H. M. Wong, "Evaluating flow-field and expelled droplets in the mockup dental clinic during the COVID-19 pandemic," *Phys. Fluids* **33**, 047111 (2021).
- ³⁹M. Abuhegazy, K. Talaat, O. Anderoglu, and S. V. Poroseva, "Numerical investigation of aerosol transport in a classroom with relevance to COVID-19," *Phys. Fluids* **32**, 103311 (2020).
- ⁴⁰P. Dey, S. K. Saha, and S. Sarkar, "Study of the interactions of sneezing droplets with particulate matter in a polluted environment," *Phys. Fluids* **33**, 113310 (2021).
- ⁴¹S. H. Smith, G. A. Somsen, C. van Rijn, S. Kooij, L. van der Hoek, R. A. Bem, and D. Bonn, "Aerosol persistence in relation to possible transmission of SARS-CoV-2," *Phys. Fluids* **32**, 107108 (2020).
- ⁴²M. Zhou and J. Zou, "A dynamical overview of droplets in the transmission of respiratory infectious diseases," *Phys. Fluids* **33**, 031301 (2021).
- ⁴³Y. Zhang, T. L. Chia, and W. H. Finlay, "Experimental measurement and numerical study of particle deposition in highly idealized mouth-throat models," *Aerosol Sci. Technol.* **40**, 361–372 (2006).
- ⁴⁴M. Moller and A. Denicola, "Study of protein-ligand binding by fluorescence," *Biochem. Mol. Biol. Educ.* **30**, 309–312 (2002).
- ⁴⁵Z. Limpouchová and K. Procházka, "Theoretical principles of fluorescence spectroscopy," in *Fluorescence Studies of Polymer Containing Systems* (Springer International Publishing, Cham, 2016); available at https://link.springer.com/chapter/10.1007/978-3-319-26788-3_4
- ⁴⁶T. G. Mayerhofer, H. Mutschke, and J. Popp, "Employing theories far beyond their limits—The case of the (Boguer-) Beer-Lambert law," *ChemPhysChem* **17**, 1948–1955 (2016).
- ⁴⁷A. Sassaroli and S. Fantini, "Comment on the modified Beer-Lambert law for scattering media," *Phys. Med. Biol.* **49**, N255–N257 (2004).
- ⁴⁸Y. Zhang, W. H. Finlay, and E. A. Matida, "Particle deposition measurements and numerical simulation in a highly idealized mouth-throat," *J. Aerosol Sci.* **35**, 789–803 (2004).
- ⁴⁹T. N. Tang, H. R. Munkelwitz, and G. Davis, "Aerosol growth studies—II. Preparation and growth measurements of monodisperse salt aerosols," *J. Aerosol Sci.* **8**, 149–159 (1977).
- ⁵⁰Z. Zhang, C. Kleinstreuer, and C. S. Kim, "Water vapor transport and its effects on the deposition of hygroscopic droplets in a human upper airway model," *Aerosol Sci. Technol.* **40**, 1–16 (2006).
- ⁵¹Z. Zhang, C. Kleinstreuer, and C. S. Kim, "Isotonic and hypertonic saline droplet deposition in a human upper airway model," *J. Aerosol Med.* **19**, 184–198 (2006).
- ⁵²X. L. Chen, Y. Feng, W. Q. Zhong, and C. Kleinstreuer, "Numerical investigation of the interaction, transport and deposition of multicomponent droplets in a simple mouth-throat model," *J. Aerosol Sci.* **105**, 108–127 (2017).
- ⁵³W. H. Finlay, *The Mechanics of Inhaled Pharmaceutical Aerosols* (Academic Press, 2001).
- ⁵⁴Z. Zhang, C. Kleinstreuer, and C. S. Kim, "Effects of curved inlet tubes on air flow and particle deposition in bifurcating lung models," *J. Biomech.* **34**, 659–669 (2001).
- ⁵⁵X. L. Chen, R. Ma, W. Q. Zhong, B. B. Sun, and X. G. Zhou, "Numerical study of the effects of temperature and humidity on the transport and deposition of hygroscopic aerosols in a G3-G6 airway," *Int. J. Heat Mass Transfer* **138**, 545–552 (2019).
- ⁵⁶X. L. Chen, C. Kleinstreuer, W. Q. Zhong, Y. Feng, and X. G. Zhou, "Effects of thermal airflow and mucus-layer interaction on hygroscopic droplet deposition in a simple mouth-throat model," *Aerosol Sci. Technol.* **52**, 900–912 (2018).